

Supplementary Information

Tailoring catalytic properties of alkylation using Cu- and Fe contained mesoporous MEL zeolites

Baoyu Liu^{a,*}, Jiajin Huang^a, Jian Yan^{b,*}, Rongchang Luo^a

^aSchool of Chemical Engineering and Light Industry, Guangzhou Key Laboratory of Clean Transportation Energy Chemistry, Guangdong University of Technology, Guangzhou, Guangdong 510006, P.R. China

^bSchool of Environmental and Chemical Engineering, Foshan University, Foshan 528000, China

* Corresponding author, Email: baoyu.liu@gdut.edu.cn (Baoyu Liu)

* Corresponding author, Email: yanjian@fosu.edu.cn (Jian Yan)

S.1 Experimental Procedures

Catalyst Preparation

Typically, the TEOS (Tetraethyl orthosilicate) was mixed with the TBAOH (Tetrabutylammonium Hydroxide) solution and aged at room temperature for 6 h with vigorous stirring, followed by the addition of iron citrate, copper acetylacetonate and deionized water. The molar composition of the final mixture was 4 TEOS : 1 TBAOH : 100 H₂O : x Fe₂O₃ : 0.08 CuO ($x = 0, 0.02, 0.04$ and 0.06). Further aging for 8 h at 50 °C, the resultant mixture was transformed into a Teflon-lined stainless-steel autoclave. After crystallizing at 170 °C for 72 h, the precipitate was washed with deionized water to neutrality and then dried overnight at 100 °C. This microporous silicalite-2 samples were denoted as P-MEL@Cu (Pure silica Cu encapsulated MEL zeolite) and P-MEL@Cu/Fe (Pure silica Cu/Fe encapsulated MEL zeolite), respectively.

A partial of Cu/Fe encapsulated silicalite-2 was further handled in an organic alkali (TBAOH) solution. Typically, 0.015 M/L aluminum isopropoxide (Aladdin) was dissolved in 0.1 M/L TBAOH solution, the relationship between the amount of aqueous solution and the as-prepared P-MEL@Cu/Fe was 30 ml per 1 g. The as-prepared P-MEL@Cu/Fe was treated with an alkaline solution at 170 °C for 72 h. Similarly, the precipitate was filtered, washed with deionized water to neutrality, and dried overnight at 100 °C. Finally, after calcination in static air at 550 °C for 6 h, these samples were denoted as H-MEL@Cu (it was synthesized from P-MEL@Cu, the Si/Al ratio and the contents of Cu were shown in Table 1) or H-MEL@Cu/Fe-1, H-MEL@Cu/Fe-2 and H-MEL@Cu/Fe-3 (they were synthesized from P-MEL@Cu/Fe and the Si/Al ratio or the contents of Cu and Fe were listed in Table 1).

Catalyst Characterization

X-ray powder diffraction (XRD) patterns were identified with a Bruker D8 diffractometer with Cu K α radiation at 2 θ angle of 5°-50°. Nitrogen adsorption/desorption measurements were recorded at -196 °C on a Micromeritics ASAP2010 instrument, while the nonlocal density functional theory (NLDFT) and Barrett–Joyner–Halenda (BJH) model were employed to analyze the pore size distribution of the samples. Scanning electron micrograph (SEM) images of calcined zeolites were obtained using a Hitachi S4800 instrument under operating condition at 10 kV (acceleration voltage). Transmission Electron Microscopy (TEM) image were obtained on a JEM-2100F instrument under operating condition at 200 kV (acceleration voltage). The energy-dispersive X-ray spectroscopy (EDS) elemental mapping was recorded with a ZEISS Ultra 55 instrument. The contents of Si, Al and transition metals were determined by inductively coupled plasma optical emission spectroscopy (ICP-OES) using an OPTIMA 7000DV (Perkin Elmer) spectrometer. Temperature programmed reduction with H₂ (H₂-TPR) experiments were recorded on an AutoChem II 2920 chemisorption analyzer. Sample was pretreated under Ar flow (50 mL/min) at 500 °C for 60 min, and the temperature and detector signals was conducted in a flow of 10% H₂/Ar (50 mL/min) from 100 °C to 800 °C at a heating rate of 10 °C/min. Surface chemical analysis of transition metals was characterized by X-ray photoelectron spectroscopy (XPS) were recorded on a Thermo Fisher Escalab 250Xi instrument equipped with an Al K α micro-focused monochromator. Electron paramagnetic resonance (EPR) spectra at X-band were recorded with a Bruker EMXplus-10/12 instrument. In situ FT-IR experiments were performed on a Bruker Vertex 70 spectrometer equipped with an MCT detector cooled by

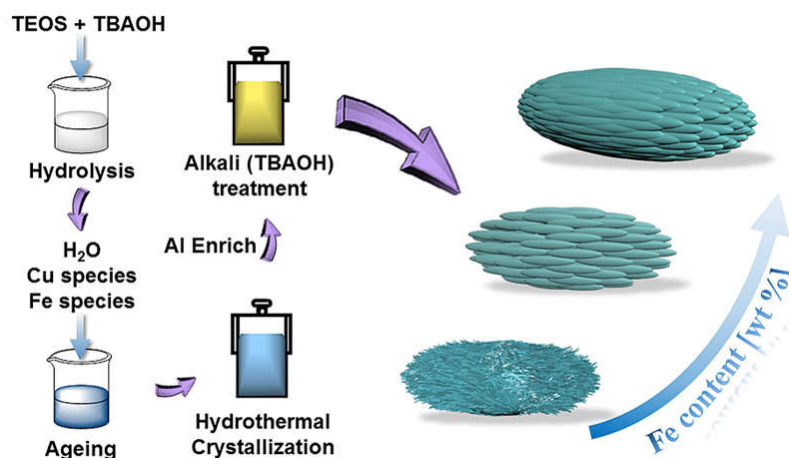
liquid nitrogen. All spectra were recorded with a resolution of 4 cm^{-1} and a scan interval of 1 min. The adsorption experiments of mesitylene were carried out in an intelligent gravimetric analyzer (IGA-003; HIDEN), which was used to determine the adsorption kinetics curves of mesitylene. The total acid concentration and the external acid amount of zeolites were detected by pyridine infrared (Py IR) and 2,6-di-tert-butyl pyridine infrared (2,6-DTBPY IR). All samples were pressed into a self-supporting wafer prior to IR measurements. The sample was degassed under vacuum at $400\text{ }^{\circ}\text{C}$ for 4 hours and cooled to room temperature in an IR cell. The total acid amount and the external acid were determined using Py and 2,6-DTBPY as probe molecules, respectively. Hereafter, the Py and 2,6-DTBPY sample wafers were adsorbed for half an hour at room temperature and degassed for 1 hour at $150\text{ }^{\circ}\text{C}$. After cooling to room temperature, the infrared spectrum was collected using a Bruker Vertex 70 spectrometer. Beer's law was used to quantitatively assess the concentration of acidic sites.¹ To calculate the total Brønsted and Lewis acid sites, the $1.67\text{ cm}^2\ \mu\text{mol}^{-1}$ and $2.22\text{ cm}^2\ \mu\text{mol}^{-1}$ as molar extinction coefficients of Py IR were employed, respectively. In addition, the molar extinction coefficient of 2,6-DTBPY IR for calculation of the external Brønsted site was $2.84\text{ cm}^2\ \mu\text{mol}^{-1}$.

DFT Calculation

The geometry optimization of compounds were carried out at using the DFT (density functional theory) method under the hybrid B3LYP function at basis set LANL2DZ with Gaussian 03 program ², and the corresponding frontier molecular orbital calculation and mulliken charge analysis were performed using the optimized structure at the B3LYP/ LANL2DZ level of theory.

Catalytic tests

Typically, liquid-phase alkylation reaction was carried out in a three-necked round bottom flask. Firstly, 40 mmol of mesitylene was added to 100 mg of the zeolite catalyst that was activated at 100 °C for 4 hours prior to reaction, and the reaction mixture was kept at 100 °C for 0.5 hours under stirring. Secondly, 4 mmol of benzyl alcohol was added, and the time was regarded as the initial reaction time. Finally, the reaction mixture was periodically taken out, and analyzed by a gas chromatograph (Agilent 7820A) with a methylsiloxane capillary column (HP-1) connected to a flame ionization detector (FID).



Scheme S1. Schematic illustration of synthesis strategy

S.2 Characterization Results of Zeolites

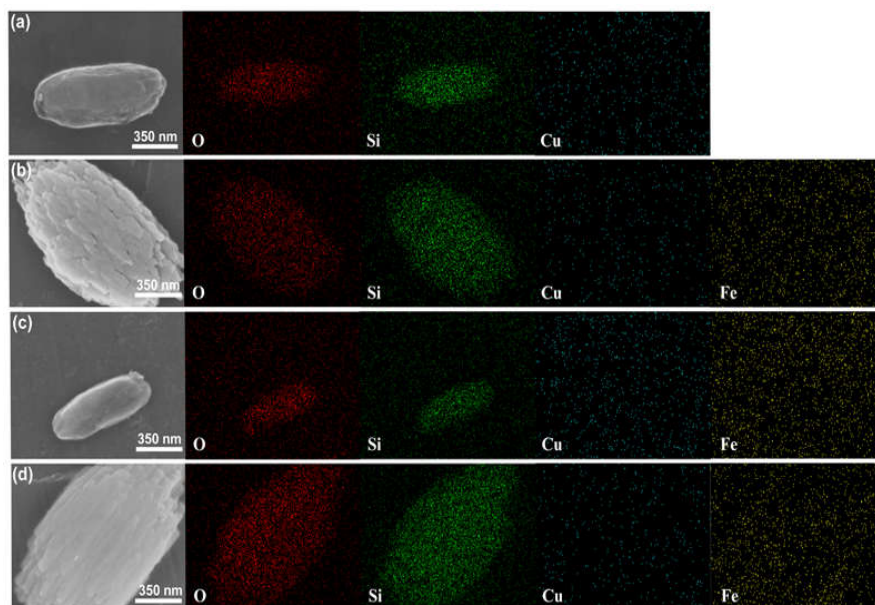


Figure S1. EDS mapping image of (a) H-MEL@Cu, (b) H-MEL@Cu/Fe-1, (c) H-MEL@Cu/Fe-2 and (d) H-MEL@Cu/Fe-3.

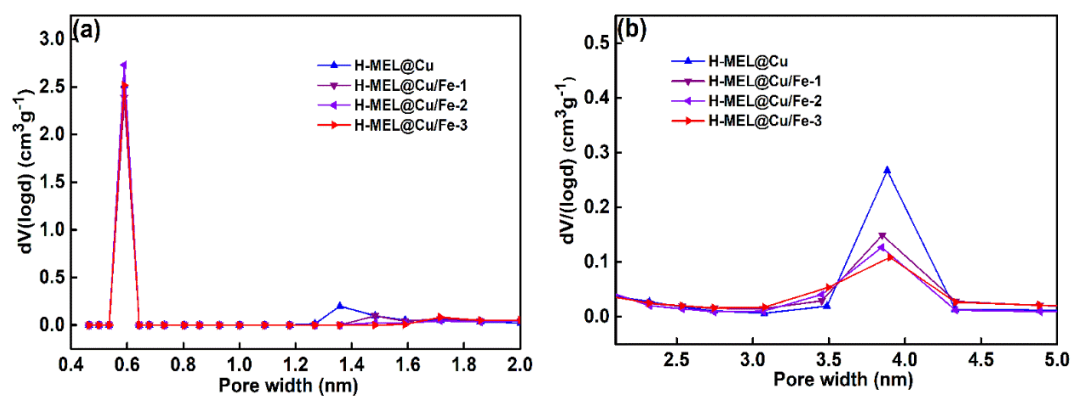


Figure S2. NLDFT (a) and BJH (b) pore size distributions of different MEL zeolite samples.

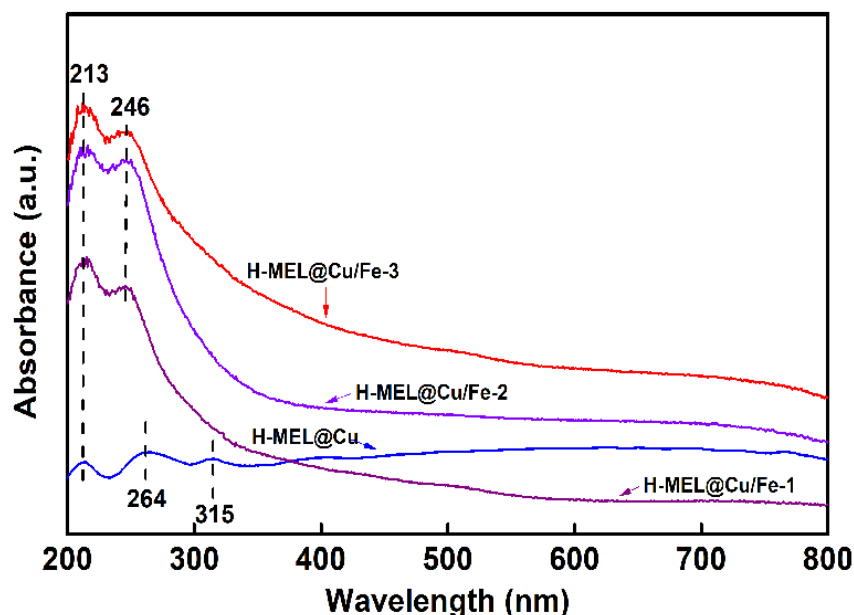


Figure S3. UV-vis spectra of (a) H-MEL@Cu, (b) H-MEL@Cu/Fe-1, (c) H-MEL@Cu/Fe-2 and (d) H-MEL@Cu/Fe-3.

Note: To obtain more information about the active ingredients of the metal, the samples were studied by UV-vis spectroscopy. For the H-MEL@Cu sample, the absorption band at ~213 nm corresponded to the isolated Cu^{2+} ions due to $\text{O}^{2-} \rightarrow \text{Cu}^{2+}$ charge transfer³. The peak at ~264 nm was related to Cu^{2+} ions⁴. In addition, an adsorption band near 315 nm indicated the presence of an oligomer species [$\text{Cu}^{2+}\text{-O}^{2-}\text{-Cu}^{2+}$] and Cu(II)-O^- ^{5, 6}. Furthermore, the wide absorption of 380-800 nm was attributed to the bulky CuO aggregation⁷. For Fe encapsulated samples, < 300 nm peaks can be attributed to isolated Fe in the framework position, 300-400 nm for oligonuclear $\text{Fe}^{3+}_x\text{O}_y$ clusters, and > 400 nm for Fe_2O_3 particles⁸. It was seen from Figure S3 that the main adsorption band was less than 300 nm, indicating that Fe species in the H-MEL@Cu/Fe-1, H-MEL@Cu/Fe-2 and H-MEL@Cu/Fe-3 mainly existed in the form of isolated Fe^{3+} . In addition, it was worth noting that the adsorption band at 213 nm was assigned to the isolated Cu^{2+} ions.

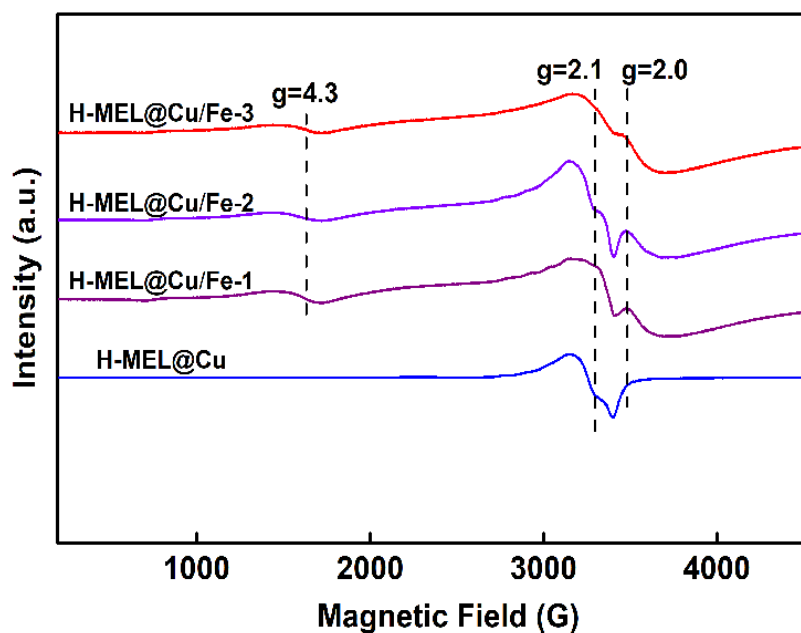


Figure S4. EPR spectra of (a) H-MEL@Cu, (b) H-MEL@Cu/Fe-1, (c) H-MEL@Cu/Fe-2 and (d) H-MEL@Cu/Fe-3.

Note: Single EPR signal at $g = 2.1$ on H-MEL@Cu sample was attributed to Cu(II) species⁹⁻¹¹. For H-MEL@Cu/Fe- x MEL zeolites, the EPR spectra showed three signals, the signals $g = 2.0$ and $g = 4.3$ were derived from highly symmetric isolated Fe ions or oligomeric clusters and tetrahedral coordination Fe(III) species, respectively^{12, 13}. In addition, the signal $g = 2.0$ overlapping with the signal $g = 2.1$ was attributed to the Cu(II) species.

S.3 Catalytic Performance of Zeolites

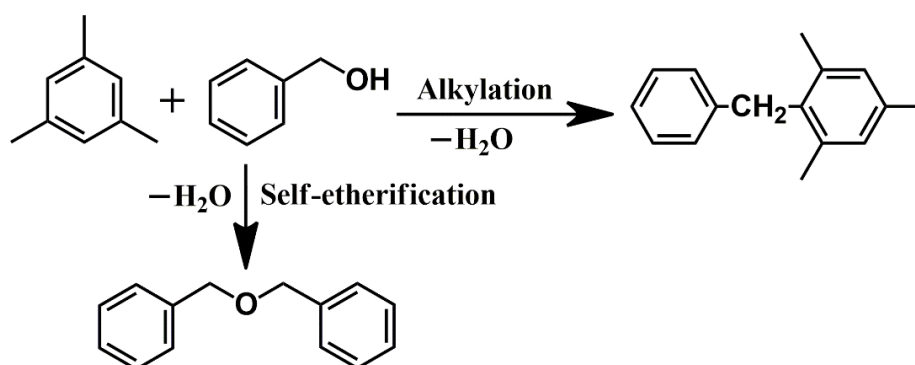


Figure S5. Friedel-Crafts alkylation of mesitylene with benzyl alcohol.

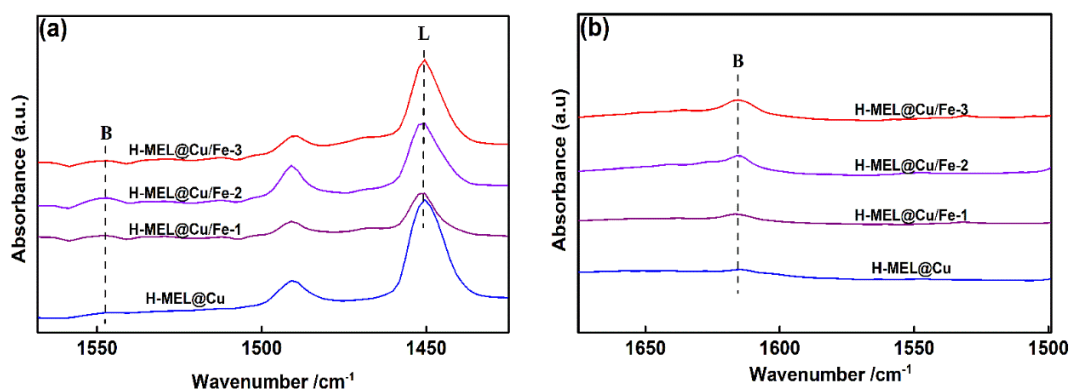


Figure S6. FTIR spectra of pyridine (a) and 2,6-di-tert-butyl pyridine (b) adsorption on different MEL zeolite samples.

Note: Here, the acidity of the zeolite samples were determined by the infrared absorption of pyridine and 2,6-DTBPY on H⁺ form H-MEL@Cu/Fe zeolites. Pyridine with a sufficient small size (a kinetic diameter = ~0.5 nm) can enter the interior of MEL zeolites (0.53 × 0.54 nm) to detect internal and external acid sites.^{14, 15} As shown in Figure S6(a), The absorption of pyridine on all samples exhibited two bands at about 1546 and 1450 cm⁻¹, which were assigned to the Brønsted acid sites and Lewis acid sites, respectively.¹⁶ The acidity of obtained MEL zeolites were calculated by using Beer's law and the corresponding results were shown in Table S1.¹⁷ It can be seen from Table S1 that the Brønsted acidity of H-MEL@Cu/Fe-*x* were higher than H-MEL@Cu, and Brønsted acid sites of zeolites were from tetracoordinated Al atoms that can connect with Si atoms through the bridging oxygen in the form of Si-OH⁺-Al,¹⁸ which indicated that additional Fe species can influence the coordinated environment of Al species. In comparison, the H-MEL@Cu/Fe-*x* showed a lower Lewis acidity than H-MEL@Cu, but the Lewis acidity of H-MEL@Cu/Fe-*x* increased in the order of H-MEL@Cu/Fe-1 < H-MEL@Cu/Fe-2 < H-MEL@Cu/Fe-3. It was mentioned that the mesitylene with a kinetic diameter of ~0.87 nm cannot enter the MEL micropore channel to participate in the alkylation reaction, suggesting that the alkylation between mesitylene with benzyl alcohol can exclusively occurred on the external surface.¹⁹ The 2,6-DTBPY with a kinetic diameter of ~0.8 nm was employed as an external surface acidic probe molecule²⁰ to estimate the external Brønsted acidity of H-MEL@Cu/Fe zeolites. As shown in Figure S6(b), the band at ~1616 cm⁻¹ was characteristic of the external Brønsted acid sites, Table S1 listed the corresponding quantitative data. It can be seen from Table S1 that the external Brønsted acidity of H-MEL@Cu/Fe samples increased in the order of H-MEL@Cu < H-MEL@Cu/Fe-1 < H-MEL@Cu/Fe-2 < H-MEL@Cu/Fe-3 on a certain degree, which was consistent with aforementioned analysis of textual properties of the samples that can improve the accessibility of external surface with increasing the content of Fe species.

Table S1. Acidity of resultant MEL zeolite catalysts

Catalyst	Acid sites ^a			External acid sites ^b
	B (mmol g ⁻¹)	L (mmol g ⁻¹)	B/L ^c	B (mmol g ⁻¹)
H-MEL@Cu	0.048	0.577	0.08	0.026
H-MEL@Cu/Fe-1	0.069	0.406	0.17	0.029
H-MEL@Cu/Fe-2	0.066	0.449	0.15	0.032
H-MEL@Cu/Fe-3	0.056	0.459	0.13	0.035

^a Measured by FT-IR spectra of adsorbed pyridine.

^b Measured by FT-IR spectra of adsorbed 2,6-di-tertbutylpyridine.

^c B/L= Brønsted acid sites/Lewis acid sites.

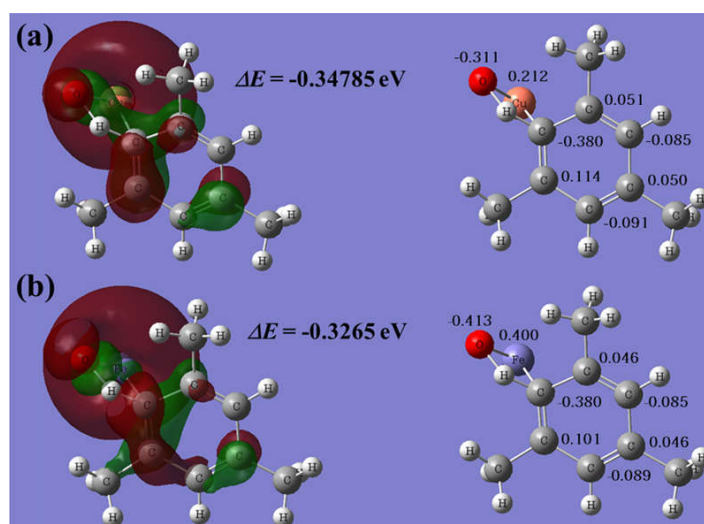


Figure S7. The highest occupied molecular orbital surfaces, mulliken charge distribution and energy levels of (a) Cu@mesitylene intermediate (b) Fe@mesitylene intermediate

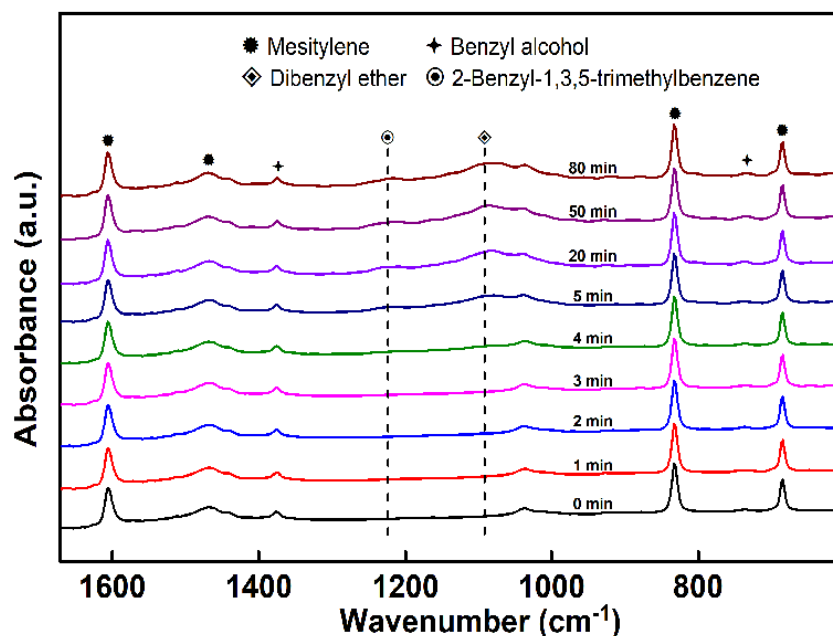


Figure S8. In situ FT-IR spectra of alkylation between mesitylene with benzyl alcohol over H-MEL@Cu/Fe-2 at various time.

Note: The intensity of the bands at $\sim 683\text{ cm}^{-1}$ and $\sim 831\text{ cm}^{-1}$ was attributed to the ring bending vibration and $=\text{C}-\text{H}$ stretching vibration of mesitylene, the peaks at $\sim 1600\text{ cm}^{-1}$ and $\sim 1470\text{ cm}^{-1}$ were caused by the $\text{C}=\text{C}$ stretching vibration of the aromatic ring skeleton of mesitylene. The band at $\sim 1090\text{ cm}^{-1}$ was assigned to the $\text{C}-\text{O}-\text{C}$ stretching vibration of dibenzyl ether, and the peak at $\sim 1225\text{ cm}^{-1}$ was arisen from the $\text{C}-\text{C}$ stretching vibration of 2-benzyl-1,3,5-trimethylbenzene. It was observed that the dibenzyl ether was gradually appeared after 5 minutes, and the corresponding 2-benzyl-1,3,5-trimethylbenzene can also be obviously found at 20 minutes, which was attributed to the fact that the main product was benzyl ether rather than 2-benzyl-1,3,5-trimethylbenzene in the initial period of reaction^{21,22}.

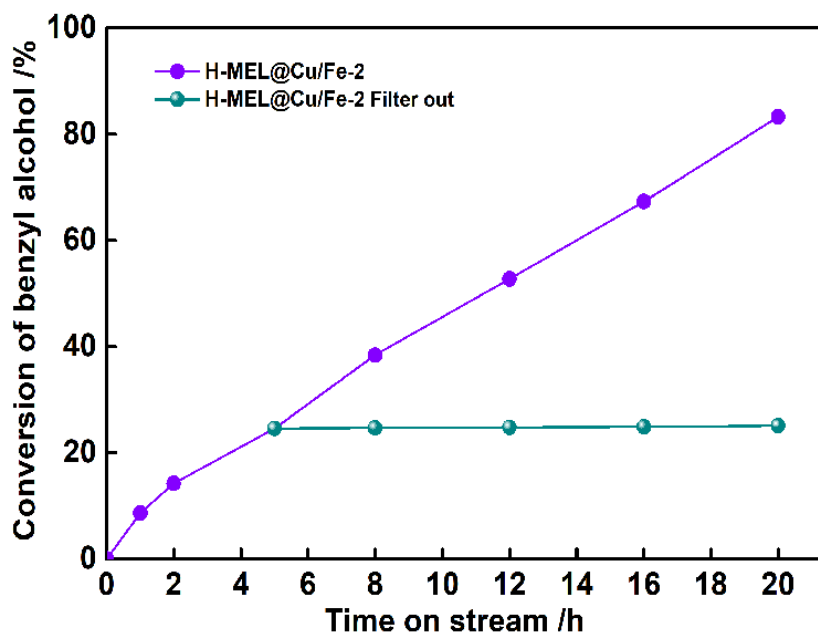


Figure S9. Leaching test of H-MEL@Cu/Fe-2.

Note: After the alkylation reaction of mesitylene and benzyl alcohol for 5 hours, the catalyst was filtered off and the reaction was continued under the same conditions. As can be seen from the Figure S9, the conversion of the reaction after the removal of the catalyst was nearly unchanged, indicating that the catalyst can strongly inhibit the leaching of loaded metal species.

S.4 Calculation of Thiele modulus (ϕ) and Effectiveness factor (η)

The Thiele modulus (ϕ) and effectiveness factor (η) were defined as depicted in Equation (1) and (2) respectively²³. Generally, the Thiele modulus and effectiveness factor were used to describe the internal diffusion limitation and catalyst utilization degree in reaction engineering.

$$\phi = \text{length} \sqrt{\frac{\text{intrinsic rate}}{\text{diffusion coefficient}}} \quad (1)$$

$$\eta = \frac{\text{measured activity}}{\text{activity without diffusion limitation}} \quad (2)$$

For a reaction with first-order reaction rate and the spherical-like catalyst particles, the Thiele modulus (ϕ) and effective factor (η) can be calculated as follows: ^{24, 25}

$$\phi = \frac{r}{3} \sqrt{\frac{k}{D}} = \frac{r}{3} \sqrt{\frac{k_{ext,alk} N_{ext,H^+} F_{ext,metal}}{D_{A,eff}}} \quad (3)$$

$$\eta = \frac{1}{\phi} \left(\frac{1}{\tanh(3\phi)} - \frac{1}{3\phi} \right) \quad (4)$$

Where r was the particle characteristic radius, measured from TEM images, k was intrinsic reaction rate constant, $D_{A,eff}$ was effective diffusion coefficient, $k_{ext,alk}$ represented the effective rate constant associated with alkylation reaction occurred on the external surface. N_{ext,H^+} was denoted the concentration of external Brønsted acid sites, $F_{ext,metal}$ was the concentration of metal active sites on external surface. The corresponding $k_{ext,alk} N_{ext,H^+} F_{ext,metal}$ and $D_{A,eff}$ parameters were calculated based on the following rate equation (9) of alkylation and adsorption kinetic curves (12).

For the investigated MEL zeolites, the alkylation of mesitylene with benzyl alcohol occurred exclusively on the external surface area. Because an excess amount of mesitylene was used (molar ratio of mesitylene to benzyl alcohol = 10:1), the alkylation can be approximated as pseudo-first order reaction ²⁶, respectively. The reaction model was established as follows: ²⁷

$$dC_B/dt = k_{ext,alk} N_{ext,H^+} F_{ext,metal} C_A \quad (5)$$

$$\tau = \frac{2C_C}{C_B} \quad (6)$$

$$C_B = \frac{C_A^0 - C_A}{1 + \tau} \quad (7)$$

By substitution of C_B (7) into equation (5), the rate equation became:

$$dC_A/dt = -k_{ext,alk} N_{ext,H^+} F_{ext,metal} (1 + \tau) C_A \quad (8)$$

Integration of equation (8) gave the rate integral form of the rate equation (9):

$$\ln \frac{C_A^0}{C_A} = k_{ext,alk} N_{ext,H^+} F_{ext,metal} (1 + \tau) t \quad (9)$$

Where C_A^0 was the initial benzyl alcohol concentration in the solution (mmol L⁻¹), C_A was the concentration of benzyl alcohol in the solution (mmol L⁻¹). The τ was the selectivity of alkylation and etherification, t was the reaction time (s), C_B and C_C were the

concentrations of 2-benzyl-1,3,5-trimethylbenzene and dibenzyl ether in solution (mol L^{-1}), respectively. The constant of the external acid sites of the alkylation reactions rate was $k_{ext,alk}$ ($\text{s}^{-1} [\text{mol H}_{ext}^+]^{-1}$). When $\ln(C_A^0/C_A)$ was plotted to t , a straight line with slope $[k_{ext,alk}N_{ext,H}+F_{ext,metal}]$ was obtained.

The effective diffusion coefficient ($D_{A,eff}$) was calculated through adsorption kinetics curves of mesitylene on the MEL zeolite. According to Fick's law, the diffusion equation was:²⁸

$$D_A \left(\frac{\partial^2 C}{\partial r^2} + \frac{2}{r} \frac{\partial C}{\partial r} \right) = \frac{\partial C}{\partial t} \quad (10)$$

Where D_A is diffusion coefficients, C is diffusion concentration, r is radial coordinates, t is the diffusion time.

When the adsorbent was considered to be a spherical particle, the mathematical solution for the transient diffusion equation can be defined as following well-known form:²⁹

$$\frac{Q_t - Q_0}{Q_e - Q_0} = 1 - \frac{6}{\pi^2} \sum_{n=1}^{\infty} \frac{1}{n^2} \exp\left(-n^2 \frac{\pi^2 D_{A,eff} t}{r^2}\right) \quad (11)$$

For short time periods, Equation (11) can be further described as:³⁰

$$\frac{Q_t - Q_0}{Q_e - Q_0} \cong \frac{6}{\sqrt{\pi}} \sqrt{\frac{D_{A,eff}}{r^2}} \sqrt{t} \quad (12)$$

Where $D_{A,eff}$ ($\text{m}^2 \text{s}^{-1}$) was the effective diffusion coefficient, r (m) was the particle radius, Q_0 was the initial weight of the adsorbent (g), Q_e and Q_t (g) were the amount of adsorbent at equilibrium and time t (s), respectively. Based on the adsorption kinetic curves (Figure S10), intra-crystalline diffusion coefficients of mesitylene within the various zeolites can be estimated³¹, the transient fractional uptakes can be described by the following equation (12) in the range of fractional uptake less than 70%. As shown in Figure S11, the $(Q_t - Q_0)/(Q_e - Q_0)$ was plotted versus \sqrt{t} , a straight line with a slope $(\frac{6}{\sqrt{\pi}} \sqrt{\frac{D_{A,eff}}{r^2}})$ can be obtained. As a result, the diffusion time constant $D_{A,eff}/r^2$ (s^{-1}) and diffusion coefficient $D_{A,eff}$ ($\text{m}^2 \text{s}^{-1}$) can be found from the slope of the line.

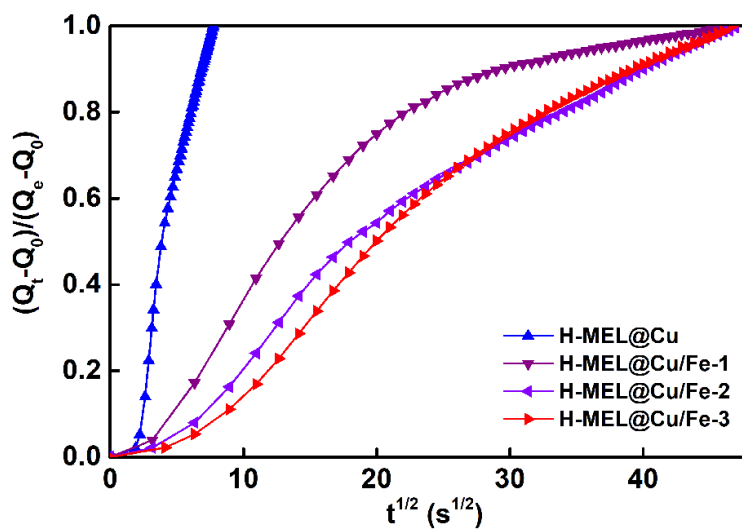


Figure S10 Mesitylene fraction adsorption uptakes on various zeolite samples

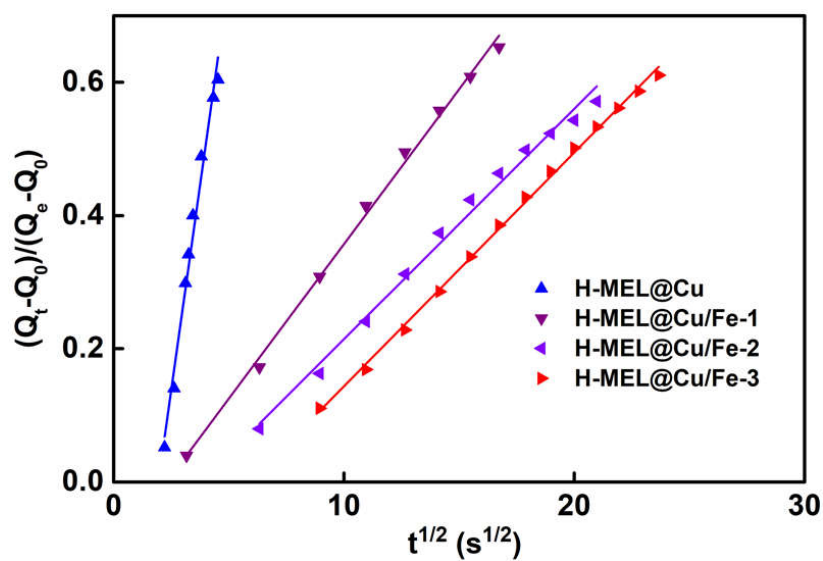


Figure S11. Plots of the fractional adsorption uptakes of mesitylene against the square root

Note: Assuming diffusion into porous spheres, the transient fraction uptakes can be described by the equation (12) in the region with uptake less than 70% ³¹.

Table S2 Parameters used in estimation of Thiele modulus in alkylation over the various zeolite catalysts

Parameters	Samples, Symbol and unit	Value
Initial benzyl alcohol concentration	C^0_A , (mol/L)	3.53×10^{-3}
	H-MEL@Cu, $D_{A,eff}/r^2$ (s^{-1})	5.28×10^{-3}
Diffusion time constant ^a	H-MEL@Cu/Fe-1, $D_{A,eff}/r^2$ (s^{-1})	0.19×10^{-3}
	H-MEL@Cu/Fe-2, $D_{A,eff}/r^2$ (s^{-1})	0.10×10^{-3}
	H-MEL@Cu/Fe-3, $D_{A,eff}/r^2$ (s^{-1})	0.11×10^{-3}
	H-MEL@Cu, r (m)	2.56×10^{-7}
Particle radius ^b	H-MEL@Cu/Fe-1, r (m)	6.05×10^{-7}
	H-MEL@Cu/Fe-2, r (m)	3.16×10^{-7}
	H-MEL@Cu/Fe-3, r (m)	6.72×10^{-7}
	H-MEL@Cu, k (s^{-1})	0.04×10^{-4}
Intrinsic reaction rate constant ^c	H-MEL@Cu/Fe-1, k (s^{-1})	0.10×10^{-4}
	H-MEL@Cu/Fe-2, k (s^{-1})	0.14×10^{-4}
	H-MEL@Cu/Fe-3, k (s^{-1})	0.18×10^{-4}

^aThe diffusion time constant was obtained based on the slop shown in Fig. S10, ^bParticle radius was calculated as the equal to the volume of sphere ²⁵, ^cIntrinsic reaction rate constant was calculated by the equation (3) and (9).

Note: It was observed that diffusion time constants for the resultant zeolite samples were in the range of $10^{-3} \sim 10^{-5}$, indicating that the diffusion of mesitylene molecules within the channels of zeolites was intra-crystalline diffusion rather than the inter-crystalline diffusion ³². In addition, the H-MEL@Cu exhibited larger diffusion time constant than H-MEL@Cu/Fe-*x*, suggesting that Cu species were beneficial to improving the adsorption of mesitylene and additional Fe species weakened the adsorption of mesitylene owing to the partial coverage of Cu species by Fe species, which was in agreement with analysis of DFT calculation and H₂-TPR results.

References

1. J. H. Lyu, H. L. Hu, C. Tait, J. Y. Rui, C. Y. Lou, Q. T. Wang, W. W. Han, Q. F. Zhang, Z. Y. Pan and X. N. Li, Benzene alkylation with methanol over phosphate modified hierarchical porous ZSM-5 with tailored acidity, *Chin. J. Chem. Eng.*, 2017, 25, 1187-1194.
2. B. Y. Liu, Z. Liu, G. C. Han and Y. H. Li, Synthesis, spectroscopic properties, crystal structure and density functional studies of Cu(II) complex with 2-((dehydroabietylamine)methyl)-6-methoxyphenol, *J. Mol. Struct.*, 2010, 975, 194-199.
3. K. Lee, H. Kosaka, S. Sato, T. Yokoi, B. Choi and D. Kim, Effects of Cu loading and zeolite topology on the selective catalytic reduction with C₃H₆ over Cu/zeolite catalysts, *J. Ind. Eng. Chem.*, 2019, 72, 73-86.
4. H. Wang, R. Xu, Y. Jin and R. Zhang, Zeolite structure effects on Cu active center, SCR performance and stability of Cu-zeolite catalysts, *Catal. Today*, 2019, 327, 295-307.
5. L. Emdadi, Y. Q. Wu, G. H. Zhu, C. C. Chang, W. Fan, T. Pham, R. F. Lobo and D. X. Liu, Dual Template Synthesis of Meso- and Microporous MFI Zeolite Nanosheet Assemblies with Tailored Activity in Catalytic Reactions, *Chem. Mater*, 2014, 26, 1345-1355.
6. Y. Itho, S. Nishiyama, S. Tsuruya and M. Masai, Redox behavior and mobility of copper ions in NaZSM-5 zeolite during oxidation, *J. Phys. Chem*, 1994, 98, 960-967.
7. W. Zhang, J. Y. Xie, W. Hou, Y. Q. Liu, Y. Zhou and J. Wang, One-Pot Template-Free Synthesis of Cu-MOR Zeolite toward Efficient Catalyst Support for Aerobic Oxidation of 5-Hydroxymethylfurfural under Ambient Pressure, *Acs Appl. Mater. Interfaces*, 2016, 8, 23122-23132.
8. C. Dai, A. Zhang, M. Liu, L. Gu, X. Guo and C. Song, Hollow Alveolus-Like Nanovesicle Assembly with Metal-Encapsulated Hollow Zeolite Nanocrystals, *ACS nano*, 2016, 10, 7401.
9. R. Baran, F. Averseng, D. Wierzbicki, K. Chalupka, J.-M. Krafft, T. Grzybek and S. Dzwigaj, Effect of postsynthesis preparation procedure on the state of copper in CuBEA zeolites and its catalytic properties in SCR of NO with NH₃, *Appl. Catal., A*, 2016, 523, 332-342.
10. T. Zhang, J. M. Li, J. Liu, D. X. Wang, Z. Zhao, K. Cheng and J. H. Li, High activity and wide temperature window of Fe-Cu-SSZ-13 in the selective catalytic reduction of NO with ammonia, *AIChE J.*, 2015, 61, 3825-3837.
11. C. Bian, Y.-N. Zhou and Z.-H. Luo, Mechanistic and kinetic investigation of Cu(II)-catalyzed controlled radical polymerization enabled by ultrasound irradiation, *AIChE J.*, 2019, 66, e16746.
12. Y. J. Chen, C. Li, X. Chen, Y. Liu, C. W. Tsang and C. H. Liang, Synthesis and Characterization of Iron-Substituted ZSM-23 Zeolite Catalysts with Highly Selective Hydroisomerization of n-Hexadecane, *Ind. Eng. Chem. Res.*, 2018, 57, 13721-13730.
13. R. Pérez Vélez, I. Ellmers, H. Huang, U. Bentrup, V. Schünemann, W. Grünert and A. Brückner, Identifying active sites for fast NH₃-SCR of NO/NO₂ mixtures over Fe-ZSM-5 by operando EPR and UV-vis spectroscopy, *J. Catal*, 2014, 316, 103-111.
14. F. Bleken, W. Skistad, K. Barbera, M. Kustova, S. Bordiga, P. Beato, K. P. Lillerud, S. Svelle and U. Olsbye, Conversion of methanol over 10-ring zeolites with differing volumes at channel intersections: comparison of TNU-9, IM-5, ZSM-11 and ZSM-5, *Phys. Chem. Chem. Phys* 2011, 13, 2539-2549.
15. H. S. Shin, M. Opanasenko, C. P. Cabello, R. Ryoo and J. Cejka, Surfactant-directed mesoporous zeolites with enhanced catalytic activity in tetrahydropyranylation of alcohols: Effect of framework type and morphology, *Appl Catal A*, 2017, 537, 24-32.

16. V. V. Ordonsky, V. Y. Murzin, Y. V. Monakhova, Y. V. Zubavichus, E. E. Knyazeva, N. S. Nesterenko and I. I. Ivanova, Nature, strength and accessibility of acid sites in micro/mesoporous catalysts obtained by recrystallization of zeolite BEA, *Microporous Mesoporous Mater*, 2007, 105, 101-110.
17. F. Cataldo, S. Iglesias-Groth, D. A. Garcia-Hernandez and A. Manchado, Determination of the Integrated Molar Absorptivity and Molar Extinction Coefficient of Hydrogenated Fullerenes, *Fuller. Nanotub. Car N*, 2013, 21, 417-428.
18. Y. Seo, K. Cho, Y. Jung and R. Ryoo, Characterization of the Surface Acidity of MFI Zeolite Nanosheets by ³¹P NMR of Adsorbed Phosphine Oxides and Catalytic Cracking of Decalin, *ACS Catal*, 2013, 3, 713-720.
19. L. Emdadi, S. C. Oh, Y. Q. Wu, S. N. Oliaee, Y. X. Diao, G. H. Zhu and D. X. Liu, The role of external acidity of meso-/microporous zeolites in determining selectivity for acid-catalyzed reactions of benzyl alcohol, *J. Catal*, 2016, 335, 165-174.
20. A. Corma, V. Fornes, L. Forni, F. Marquez, J. Martinez-Triguero and D. Moscotti, 2,6-di-tert-butyl-pyridine as a probe molecule to measure external acidity of zeolites, *J. Catal*, 1998, 179, 451-458.
21. A. B. Deshpande, A. R. Bajpai and S. D. Samant, The enhanced activity of Sb after supporting on K10 in the benzylation of benzene using benzyl chloride and benzyl alcohol, *Appl. Catal., A*, 2001, 209, 229-235.
22. T. Yamato, C. Hideshima, G. K. S. Prakash and G. A. Olah, Solid Superacid-Catalyzed Organic-Synthesis .4. Perfluorinated Resinsulfonic Acid (Nafion-H) Catalyzed Friedel-Crafts Benzylation of Benzene and Substituted Benzenes, *J Org Chem*, 1991, 56, 2089-2091.
23. D. Liu, A. Bhan, M. Tsapatsis and S. Al Hashimi, Catalytic Behavior of Brønsted Acid Sites in MWW and MFI Zeolites with Dual Meso- and Microporosity, *ACS Catal*, 2011, 1, 7-17.
24. M. Hartmann, A. G. Machoke and W. Schwieger, Catalytic test reactions for the evaluation of hierarchical zeolites, *Chem. Soc. Rev*, 2016, 45, 3313-3330.
25. D. Xu, O. Abdelrahman, S. H. Ahn, Y. Guefrachi, A. Kuznetsov, L. Ren, S. Hwang, M. Khaleel, S. Al Hassan, D. Liu, S. B. Hong, P. Dauenhauer and M. Tsapatsis, A quantitative study of the structure–activity relationship in hierarchical zeolites using liquid-phase reactions, *AIChE J*, 2019, 65, 1067-1075.
26. L. Emdadi, S. C. Oh, Y. Wu, S. N. Oliaee, Y. Diao, G. Zhu and D. Liu, The role of external acidity of meso-/microporous zeolites in determining selectivity for acid-catalyzed reactions of benzyl alcohol, *J. Catal*, 2016, 335, 165-174.
27. L. Emdadi, Y. Wu, G. Zhu, C.-C. Chang, W. Fan, T. Pham, R. F. Lobo and D. Liu, Dual Template Synthesis of Meso- and Microporous MFI Zeolite Nanosheet Assemblies with Tailored Activity in Catalytic Reactions, *Chem. Mater*, 2014, 26, 1345-1355.
28. J. Gou, Z. Wang, C. Li, X. Qi, V. Vattipalli, Y.-T. Cheng, G. Huber, W. C. Conner, P. J. Dauenhauer, T. J. Mountziaris and W. Fan, The effects of ZSM-5 mesoporosity and morphology on the catalytic fast pyrolysis of furan, *Green Chem*, 2017, 19, 3549-3557.
29. Z. H. S. L. Q. Y. D. L. S. Zhaolin, Adsorption Thermodynamics and Diffusion Kinetics of PX over NaY Zeolite Synthesized by in-situ Crystallization from Kaolin Microsphere, *China Petrol Proc & Petrochem Techn*, 2014, 16, 47-54.
30. F. Xu, S. Xian, Q. Xia, Y. Li and Z. Li, Effect of Textural Properties on the Adsorption and Desorption of Toluene on the Metal-Organic Frameworks HKUST-1 and MIL-101, *Adsorpt. Sci. Technol*, 2013, 31, 325-339.
31. Z. Zhao, Z. Li and Y. S. Lin, Adsorption and Diffusion of Carbon Dioxide on Metal–Organic Framework (MOF-5), *Ind. Eng. Chem. Res*, 2009, 48, 10015-10020.
32. C.-C. Chang, A. R. Teixeira, C. Li, P. J. Dauenhauer and W. Fan, Enhanced Molecular Transport in Hierarchical Silicalite-1, *Langmuir*, 2013, 29, 13943-13950.